Title

High-pressure polymorphism of PbF2 to 75 GPa



Journal

Physical Review B, 94(2)

ISSN

2469-9950

Authors

Stan, Camelia V

Dutta, Rajkrishna

White, Claire E

et al.

Publication Date

2016-07-01

DOI

10.1103/physrevb.94.024104

Peer reviewed

# High-pressure polymorphism of $PbF_2$ to 75 GPa

Camelia V. Stan[1], Rajkrishna Dutta[2], Claire E. White[3,4], Vitali Prakapenka[5], Thomas S. Duffy[2]

1. Department of Chemistry, Princeton University, Princeton, NJ 08544, USA

2. Department of Geosciences, Princeton University, Princeton, NJ 08544, USA

3. Department of Civil and Environmental Engineering, Princeton University, NJ-08544, USA.

4. Andlinger Center for Energy and the Environment, Princeton University, NJ-08544, USA.

5. GeoSoilEnviroCARS, University of Chicago, Argonne National Lab, Argonne, IL 60439, USA

**Abstract**

Lead fluoride, $PbF_2$, was investigated experimentally in the laser-heated diamond anvil cell by x-ray diffraction to pressures of 75 GPa at room temperature and to 64.5 GPa and 2430 K, as well as through first-principles density functional theory calculations up to 70 GPa. During room temperature compression, no discontinuous changes in the x-ray diffraction pattern or volume were observed, but the lattice parameters display highly anomalous trends between 10-22 GPa with enhanced compressibility along the *a* direction and reduced or even negative compressibility along *b* and *c*. Theoretical calculations of valence electron densities at 22 GPa show that α-$PbF_2$ has undergone a pressure-induced isosymmetric phase transition to a post-cotunnite $Co_2Si$-type structure and also reveal the detailed atomic rearrangements associated with the development of an extra Pb-F bond in the high-pressure phase. Our x-ray results and theoretical calculations are consistent with an isosymmetric phase transition occurring over 10-22 GPa rather than abruptly as previously suggested. The characteristic values for the cell constants $a/c$ and $(a+c)/b$ which are used to distinguish among cotunnite-, $Co_2Si$-, and $Ni_2In$-type phases require modification based on our results. An equation of state fit yields a bulk modulus,

$K_0$, of 72(3) GPa for cotunnite, and an ambient-pressure volume, $V_0$, of 182(2) Å$^3$, and $K_0$ = 81(4) GPa for $Co_2Si$-type phase when fixing the pressure derivative of the bulk modulus, $K_0$'= 4. Upon heating above 1200 K at pressures at or above 25.9 GPa, $PbF_2$ partially transforms to the hexagonal $Ni_2In$-type phase but wholly or partially reverts back to $Co_2Si$-type phase upon temperature quench. From 43-65 GPa, nearly complete transformation to the $Ni_2In$-type $PbF_2$ is observed at high temperature, but the material partially transforms back to the orthorhombic phase upon temperature quench. Our results show that high-pressure behavior of $PbF_2$ is distinct from that of the alkaline earth fluorides with similar ionic radii. Our results also have relevance to understanding the behavior of lanthanide and actinide dioxides, which have been predicted theoretically to exhibit similar isosymmetric transitions at Mbar pressures.

## I. INTRODUCTION

The high-pressure behavior of compounds in the $AX_2$ family has attracted much attention due to their extensive polymorphism, highly coordinated structures, and diverse transformation pathways [1]. Lead fluoride, $PbF_2$, is a difluoride which has attracted strong interest due to its technological applications [2–4] and its high-pressure polymorphism [5,6].

At ambient conditions $PbF_2$ crystallizes in the cubic fluorite structure (β-$PbF_2$, $Fm\bar{3}m$) in which Pb is in 8-fold coordination with fluorine. At 0.4 GPa, it undergoes a phase transition to an orthorhombic 9-fold coordinated cotunnite structure (α-$PbF_2$, *Pnma*), which remains metastable when quenched to ambient pressure for T < 610 K [7]. Other metal dihalides also adopt the cotunnite structure, and exhibit varied polymorphism upon compression at ambient and high temperatures [5,8–14]. For instance, the difluorides $CaF_2$, $SrF_2$ and $BaF_2$ undergo a transition from cotunnite to 11-fold coordinated $Ni_2In$-type structure ($P6_3/mmc$) at pressures that

scale with cation size [13,14]. Difluorides have been found to be good analogs for the high-pressure behavior of oxides due to the their lower transition pressures [14]. $SiO_2$ is predicted to adopt the cotunnite structure at ultrahigh pressures of ~700 GPa [15,16], which would correspond to conditions deep in the interior of large, earth-like extrasolar planets [17]. Additionally, a number of metal dioxides including $TiO_2$, $ZrO_2$, $HfO_2$, $SnO_2$, $PbO_2$, $CeO_2$, $PuO_2$, $UO_2$ and $ThO_2$ are known or predicted to adopt the cotunnite or related structures at elevated pressures, leading to phases with very high bulk moduli or unusual compressibilities [18–25].

The high-pressure post-cotunnite phase of $PbF_2$ has been controversial. In an X-ray diffraction study, Haines *et al*. [5] suggest an isosymmetric phase transition to a "$Co_2Si$-related" structure at 12.9 GPa. Their analysis is based entirely on empirical observations of characteristic lattice parameter ratios for the cotunnite-type, $Co_2Si$-type and $Ni_2In$-type phases [13,26]. On the other hand, quantum mechanical calculations based on the *ab initio* perturbed ion method predict that the post-cotunnite phase in $PbF_2$ is the $Ni_2In$-type structure [27]. A joint experimental and theoretical study discovered a structural transformation at 14.7 GPa, but the structure of the high-pressure phase could not be determined [6].

The cotunnite-type, $Co_2Si$-type, and $Ni_2In$-type structures occur over a wide range of compositions and are closely related structurally [28]. Each is based on a distorted hexagonal close packed arrangement of anions with cations in face-sharing polyhedra forming corrugated sheets. The cation coordination polyhedra are multi-capped trigonal prisms, where the number of caps increases with coordination number in sequence. Thus, the cotunnite-type phase (9-fold coordination) is tri-capped, $Co_2Si$ (10-fold coordination) is tetra-capped and $Ni_2In$ (11-fold coordination) is penta-capped (Fig. 1). All caps are located along the rectangular faces of the trigonal prisms, which form corrugated layers that are stacked along the *b* direction. While the

cotunnite-type and a $Co_2Si$-like structure have been reported previously in $PbF_2$ [5] and theoretical calculations suggest that $Ni_2In$-type $PbF_2$ should be stable at higher pressures [27], $Ni_2In$-type $PbF_2$ has not been synthesized to date, and no simultaneous high-pressure and temperature experimental studies have been reported as yet.

## II. METHODS

### A. High-pressure experiments

Polycrystalline $PbF_2$ (Alfa Aesar, >99% purity) was examined by x-ray diffraction at ambient conditions and indexed as the orthorhombic cotunnite-type phase with the unit cell $a$ = 6.4472(3) Å, $b$ = 3.9019(2) Å, $c$ = 7.6514(3) Å and $V$ = 192.48(1) Å$^3$. The sample was ground to micron-sized grains and mixed with 10-15 wt.% platinum which was used as a pressure calibrant and laser absorber. The mixture was pressed into a thin layer and loaded into piston-cylinder type diamond anvil cells using either NaCl or Ne as pressure-transmitting media. In one experiment, a small foil of Pt metal was loaded adjacent to pure $PbF_2$ powder, and in another, 5 wt.% graphite was mixed in the sample as a laser absorber instead of Pt. This was done in order to eliminate overlap between the sample and Pt peaks in the diffraction patterns between 7-15 GPa. Diamond anvils with culet sizes of 200-500 μm were mounted on tungsten carbide or cubic boron nitride seats. Sample chambers were formed by drilling holes in Re gaskets that were pre-indented to 20-30 μm thickness. The holes were approximately half the diameter of the diamond culet.

Angle-dispersive x-ray diffraction experiments were performed at beamline 13-ID-D (GSECARS) of the Advanced Photon Source APS, Argonne National Laboratory. A monochromatic x-ray beam with λ = 0.3344 Å was focused using Kirkpatrick-Baez mirrors to a size of approximately 4 μm x 4 μm onto the sample. Diffracted x-rays were recorded using a

Mar165 CCD detector. The distance and orientation of the detector was determined using $CeO_2$ or $LaB_6$ as standards. The two-dimensional CCD images were radially integrated using the programs FIT2D [29] or DIOPTAS [30] to produce one-dimensional diffraction patterns. High-temperature experiments were carried out using a double-sided laser heating system consisting of two near-infrared diode-pumped single-mode ytterbium fiber lasers. Beam-shaping optics were used to produce a flat-topped laser profile with a spot size of ~24 μm. Sample temperatures were measured from both sides by spectroradiometry. The incident laser power was adjusted to keep the measured temperature difference from the two sides of the cell to less than 100 K. Further details of the x-ray diffraction and laser heating systems at 13-ID-D are reported elsewhere [31].

X-ray diffraction peaks were fit using non-linear least squares to background-subtracted pseudo-Voigt line profiles. Lattice parameters were obtained from measured peak positions using the program UNITCELL [32]. Pressure was determined from the equation of state of platinum using its (111) diffraction line [33]. Equation of state fits were performed using the program EosFit7 [34].

### B. Computational details

Our theoretical calculations were restricted to the cotunnite and the post-cotunnite phases of lead fluoride. The ambient-pressure fluorite structure has not been considered, i.e., we have taken orthorhombic cotunnite to be the ambient-pressure phase. Total energy calculations were carried within the framework of density functional theory (DFT) [35,36] as implemented in the CASTEP code [37]. We used a kinetic energy cutoff of 400 eV for the plane wave basis set, while the self-consistency convergence was set to $10^{-6}$ eV. The electron-ion interactions were treated using ultrasoft pseudopotentials [38] with valence configurations of $2s^2 2p^5$ and $5d^{10} 6s^2 6p^2$ for F and Pb respectively. The exchange-correlation potentials for the electron-electron interactions were

treated in the local density approximation (LDA) [39]. The Brillouin zone was sampled using a Monkhorst-Pack [40] grid, with a separation of 0.07/Å between the *k*-points. All structural optimizations were carried out using the Broyden–Fletcher–Goldfarb–Shanno (BFGS) technique and was considered complete when the forces on atoms were less than 0.01 eV/Å and the energy change was 5 x $10^{-6}$ eV/ Å [41]. Both lattice parameters and atomic positions were relaxed at each pressure step with unconstrained symmetry.

The cotunnite structure can be described completely using nine degrees of freedom, i.e., the three lattice constants, *a*, *b*, c and six atomic coordinates ($Pb_x$, $Pb_z$, $F1_x$, $F1_z$, $F2_x$ and $F2_z$, where the subscripts indicate the non-symmetry-constrained coordinate directions of the respective atoms). In Table I, we have compared the values obtained from our theoretical calculations at ambient pressure for the nine degrees of freedom to other results from experiment and theory [5,42,43]. LDA, as expected, underestimates the lattice parameters in comparison to the experimental values and the differences are 2.2%, 2.6% and 1.2% for *a*, *b* and *c* respectively. Considering the overbinding inherent in the local density approximation [44] our results are consistent with experimental data.

## III. RESULTS

### A. Static compression of $PbF_2$

X-ray diffraction experiments were carried out at ambient temperature to 75 GPa. The diffraction peaks evolved under compression towards smaller *d*-spacings but no new peaks were observed over the measured pressure range (Fig. 2). An impurity peak belonging to Pb metal was seen with varying intensity in some patterns, but disappeared above 18 GPa where Pb undergoes a phase transition. A notable feature of the dataset was that the (200) and (211) diffraction lines

of $PbF_2$ exhibit a remarkably rapid shift in *d*-spacing as a function of pressure relative to other diffraction lines, indicating a highly anisotropic compressibility (Fig. 3). The lattice parameters and volume of $PbF_2$ were fit using an orthorhombic cell over the measured pressure range.

Theoretical calculations of the unit cell volume and lattice parameters at 0 K were also carried out. The structures were completely relaxed at each pressure step with unconstrained symmetry. Within the pressure range considered here (0 – 70 GPa), the structures maintained the same symmetry (orthorhombic, *Pnma*).

The measured and calculated lattice parameters of $PbF_2$ as a function of pressure are presented in Fig. 4. The compressional regime can be broadly divided into three regions. In the low-pressure range (0-10 GPa), the behavior is monotonic whereby all three lattice constants decrease nearly linearly with pressure. The pressure range from 10-22 GPa defines a transition region in which the response of the lattice parameters to compression is anomalous in the sense that *a* decreases with a steep gradient, while *b* and *c* slightly increase with pressure. Above 22 GPa, the lattice parameters again decrease monotonically. The theoretical and experimental results agree well in relative compression. Despite the large amount of anisotropy in the axial compressibilities, the pressure-volume curves from both theory and experiment exhibit a smooth variation over the pressure range without any sharp discontinuity (Fig. 5). Decompression experiments showed that the variation in cell volume and lattice parameters is reversible with little hysteresis.

### B. High temperature x-ray diffraction

$PbF_2$ samples were laser heated to 1000-2430 K at pressures from 16-64.5 GPa. Up to 25 GPa, there was no change in the $PbF_2$ diffraction pattern upon heating to 1400 K, but a new peak was observed that we attribute to the reaction of impurity Pb with the platinum pressure standard,

forming a face-centered cubic $Pt_3Pb$ compound [45]. At 25.9 GPa, new, weak peaks were observed within 40 seconds after the beginning of heating. These peaks are consistent with the $Ni_2In$-type phase of $PbF_2$. As far as we are aware, this is the first study to report synthesis of the $Ni_2In$-type phase in $PbF_2$. The $Ni_2In$-type peaks grew in intensity with additional heating over ~6-9 minutes (Fig. 6). Peaks corresponding to the $Co_2Si$-type phase remained present together with $Ni_2In$-type peaks throughout the heating cycle at this pressure. A diffraction pattern recorded immediately upon temperature quench showed only peaks corresponding to the $Co_2Si$-type phase while those of the $Ni_2In$-type phase had disappeared (Fig. 6).

At 30.1 GPa, growth of the $Ni_2In$ phase together with continued persistence of peaks of the low-temperature phase was observed starting from 1250 K, the lowest temperature measured. The intensity of the $Ni_2In$-type peaks grew compared to those of the $Co_2Si$-type phase as a function of increasing temperature up to 2430 K, at which point the $Ni_2In$-type peaks were much more intense than those of the $Co_2Si$-type. However, even after heating for over 20 minutes, the $Co_2Si$-type peaks did not completely disappear. Upon temperature quench, the $Ni_2In$-type peaks once again immediately disappeared and only the $Co_2Si$-type peaks were observed, similar to the observation at 25.9 GPa.

At 34 GPa, the $Ni_2In$-type peaks were again much stronger than the $Co_2Si$-type peaks during heating but upon temperature quench the $Co_2Si$ phase returned and weak peaks of the $Ni_2In$-type phase were observed (Fig. 7). At pressures above 43 GPa, nearly single-phase $Ni_2In$-type was synthesized at 1400 K, partially reverting to $Co_2Si$-type on temperature quench (Fig. 8).

## IV. DISCUSSION

### A. Static compression and equation of state

The anomalous compression behavior observed in both the x-ray diffraction and theoretical calculations is generally consistent with prior experiments on $PbF_2$ covering more limited pressure ranges (Figs. 4,5) [5,42]. To explain the anomalous compression behavior, Haines *et al*. [5] proposed an isosymmetric phase transition between 10 and 13 GPa from cotunnite-type $PbF_2$ to a "$Co_2Si$-like" structure, accompanied by a ~2% volume discontinuity. Our results are broadly consistent with those of Haines *et al*. [5], indicating a change in compressibility beginning near 10 GPa in both the experimental and computational results. However we observe a second compressibility change near 22 GPa which was not recognized by Haines *et al*. [5] as it is close to the upper pressure limit of their experiment. From 22 GPa to the maximum pressure of 75 GPa, all lattice parameters exhibit smooth variation (Fig. 4). Our study demonstrates that there is a continuous evolution of lattice parameters between 10-22 GPa and, in contrast to Haines *et al*. [5], no apparent volume discontinuity (Fig. 5).

Haines *et al.* [5] reported other changes in the diffraction patterns between 10-13 GPa including the sudden appearance of peak broadening and preferred orientation. In contrast, we do not observe any abrupt broadening or significant changes in relative peak intensities over the course of the experiment. This behavior as well as the slightly higher volumes reported by Haines *et al.* [5] are likely due to their use of silicone grease as a pressure medium which becomes strongly non-hydrostatic near 12 GPa [46].

The anisotropic compression in $PbF_2$ is similar to behavior reported in the cotunnite-type phase of the alkaline earth fluorides $CaF_2$, $SrF_2$ and $BaF_2$ [14]. A negative compressibility along the *c* axis and very high compressibility along *a* is observed in these compounds. However, this change in compressibility is part of a continuous transition to the hexagonal $Ni_2In$ phase in the alkaline earth fluorides, whereas under quasi-hydrostatic conditions $PbF_2$ does not transform to

the $Ni_2In$-type structure to at least 75 GPa without the application of heating. This observation is consistent with our theoretical calculations. The unusual compressional behavior seen here is also similar to that reported in theoretical calculations for cotunnite-structured lanthanide and actinide dioxides at Mbar pressures [18–20,25] which we address in a later section.

The $PbF_2$ cotunnite and $Co_2Si$-type compression data were fit using a Birch-Murnaghan equation of state (Fig. 5) and results are reported in Table II. The ambient pressure volume, $V_0$, for the cotunnite-type phase was taken from experimental x-ray data collected here. Fitting the data between 0 and 10 GPa yields a value for the isothermal bulk modulus of $K_0$ = 72(3) GPa when the pressure derivative of the bulk modulus, $K_0$', was fixed at 4. Our bulk modulus for cotunnite structured $PbF_2$ is similar to those reported in earlier studies of $PbF_2$ [5,42] and is greater than the value of $K_0$ = 62(1) GPa obtained for the fluorite-type phase of $PbF_2$ [47]. It is also similar to values reported for the alkaline earth fluorides $CaF_2$, $SrF_2$, and $BaF_2$ [14,48]. A fit to our compression data for the $Co_2Si$-type phase between 22-75 GPa yields $V_0$ = 182(2) $Å^3$ and $K_0$ = 81(4) GPa when $K_0$'= 4 (Table II). Our experimental results thus indicate that there are only modest changes in bulk compressibility between the fluorite, cotunnite, and $Co_2Si$-type phases of $PbF_2$.

### B. High pressure-temperature behavior

The laser-heating experiments show that with increasing pressure from 25.9-64.5 GPa, greater amounts of the $Ni_2In$-type phase are observed at temperatures above 1200 K. The volume differences between the $Co_2Si$- and $Ni_2In$ type phases appear to be small (~1%), with $Ni_2In$ volumes being consistently larger at room temperature and consistently smaller at high temperature compared to those of the coexisting $Co_2Si$-type phase. Upon temperature quenching,

mixtures of $Co_2Si$-type and $Ni_2In$-type are observed, with increasing amount of the $Ni_2In$-type being retained upon quench at higher pressures. These observations may suggest a shallow, negative Clapeyron slope for the $Co_2Si$-$Ni_2In$-type phase boundary. Additionally, the extensive coexistence region for the $Co_2Si$- and $Ni_2In$-types at both high temperature and upon quench suggests the two phases are nearly equally stable and that energy differences between them are small. Similar results were reported previously for $SrF_2$: the $Ni_2In$ phase was observed at both high temperature and upon quench at 36 GPa but existed only at high temperature and reverted to the cotunnite phase upon quench at 28 GPa [14].

We do not observe the transformation to $Ni_2In$-type in $PbF_2$ when starting from the cotunnite-type structure. The $Ni_2In$-type only formed at high temperatures at or above 25.9 GPa, a pressure regime that lies above the cotunnite-$Co_2Si$-type phase transition in $PbF_2$. It should also be noted that in experiments conducted under higher degrees of differential stress, evidence for the $Ni_2In$-type phase could be observed in $PbF_2$ at ambient temperature at pressures above the cotunnite-$Co_2Si$ phase transition. This suggests that the transition is sensitive to differential stress, which is consistent with the close structural similarity of the $Co_2Si$ and $Ni_2In$ phases and provides further evidence for a small energy difference between them.

### C. Bonding and polyhedral analysis

The theoretical results provide insight into the bonding behavior of orthorhombic $PbF_2$. The calculated change with pressure of the atomic positions for the six symmetrically unconstrained coordinates in $PbF_2$ is shown in Fig. 9. As with the lattice parameter data above, we again observe three distinct regions, where the low-pressure regime (0-10 GPa) is marked by a smooth continuous increase/decrease, followed by an anomalous zone (10-22 GPa) and then another

region of monotonic increase or decrease (>22 GPa). There are two symmetrically distinct fluorine atoms in the cotunnite/$Co_2Si$ structure which are designated F1 and F2 (Fig. 1). A clear change in the slope is evident especially in case of $Pb_x$, $F2_x$, $F2_z$ in the transition region. The atomic coordinates of the second fluorine atom (F2) exhibit a greater change in position with respect to those of the first one, with $F2_z$ showing the largest displacement.

Figure 10 shows our calculations of the total electron densities along the (010) plane at different pressures. In an electron density map, sharing of the charge density indicates a covalent bond, while an ionic bond can be identified from the complete transfer of charge density to the anion. The presence of a bond can be identified from the existence of a charge density valley between two atoms. Figure 10a shows that there is no sharing of valence charge density at ambient conditions between $Pb_d$ and $F1_c$ (crystallographically equivalent to $Pb_a$ and $F1_{b2}$ below) while there is clear evidence for the presence of charge sharing at 25 GPa (indicated by the white box in Fig. 10b). Our calculations show that there is no evidence of charge sharing between the two concerned Pb and F atoms up to 22 GPa. This confirms that the $10^{th}$ Pb-F bond does not exist in the low-pressure region, while 10-coordinated $Co_2Si$-type structure is the stable phase in the high-pressure region (>22 GPa). As expected, the Pb–F bonds appear to be partially ionic and partially covalent [4].

The geometry of bonding and atomic displacements in lead fluoride at 0 and 70 GPa is presented in Fig. 11. As mentioned previously, the cotunnite structure contains two crystallographically distinct fluorine atoms, F1 and F2, at ($F1_x$, 0.25, $F1_z$) and ($F2_x$, 0.75, $F2_z$) respectively. For simplicity, we discuss changes in the structure relative to $Pb_a$. $Pb_a$ is bonded to 4 F1 atoms ($2\times F1_a$, $F1_b$, $F1_d$) and 5 F2 atoms ($F2_a$, $2\times F2_{b2}$, $2\times F2_d$). The $Co_2Si$- and $Ni_2In$-type structures are marked by extra Pb-F1 ($Pb_a$-$F1_{b2}$) and Pb-F2 ($Pb_a$-$F2_c$) bonds, respectively. From

the calculated atomic positions, the variation of bond lengths can be determined as a function of pressure (Fig. 12). As with the lattice parameters, the lengths of all 9 Pb-F bonds in the cotunnite structure decrease (or, in the case of $Pb_a$-$F2_a$, increase) smoothly up to a pressure of 10 GPa. With further increase of pressure, the longest bond, $Pb_a$-$F2_d$, shows a marked reduction in length. This is due to the symmetrically equivalent $F2_a$ (diametrically opposite to $F2_d$) moving away from $Pb_a$, leading to an increase in the $Pb_a$-$F2_a$ bond length. Also over the same pressure region, a $10^{th}$ fluorine atom, $F1_{b2}$, which initially lies well outside the tri-capped trigonal prism (TTP) about Pb, exhibits a dramatic reduction in distance relative to $Pb_a$, eventually approaching the TTP (Fig. 12). As $F1_{b2}$ moves inward, $F2_{b2}$ experiences a strong repulsion and swings away from the incoming F atom (Fig. 11). Due to symmetry constraints, this motion also causes $F2_a$ to significantly shift position. The two opposing forces along with the movement of the central $Pb_a$ atom lead to the $Pb_a$-$F2_{b2}$ bond showing relatively low compressibility in the transition interval (10-22 GPa).

After the formation of the Pb-$F1_{b2}$ bond, as seen from the electron density calculations (Fig. 10), all the bonds show a monotonic decrease with pressure including Pb-$F2_a$. Figure 12 also compares the interatomic distance of the $10^{th}$ and $11^{th}$ nearest neighbors to Pb ($Pb_a$-$F1_{b2}$ and $Pb_a$-$F2_c$, respectively) as a function of pressure. It can be seen that the slope of $Pb_a$-$F1_{b2}$ is much steeper than that of $Pb_a$-$F2_c$, especially in the transition region, indicating its tendency to form a bond. As can be seen in Fig. 11, this motion is along the *ac* plane, and the $F2_{b2}$-$Pb_a$-$F2_a$ angle widens such that the $F2_{b2}$-$F2_a$ distance increases, primarily in the *c* direction. This atomic displacement leads to the unusual observation of an increase in the *c* lattice parameter with simultaneous decrease in the *a* lattice parameter in the transition region (Fig. 4).

### D. Lattice parameter systematics

It was shown by Jeitschko [26] and Léger *et al.* [13] that the three structures under consideration (cotunnite, $Co_2Si$-type, and $Ni_2In$-type) can be distinguished by characteristic values of the unit cell ratios $a/c$ and $(a+c)/b$ [13,26]. For the $Ni_2In$-type structure, this requires transformation from a hexagonal to an orthorhombic cell as discussed below. The empirically observed ratios for cotunnite-, $Co_2Si$- and $Ni_2In$-type are $a/c$ = 0.80-0.90 and $(a+c)/b$ = 3.3-4.0, 0.66-0.74 and 3.1-3.3, and 0.70-0.78 and 2.9-3.2, respectively [5,13,26].

We have surveyed the more recent literature and compiled additional data for a wide range of compositions that adopt these structures (Fig. 13). These new data include phosphides, hydrides, sulfides, oxides, and intermetallics [5,14,26,48–96] at ambient pressure. Data for high-pressure $SrF_2$ is also included [14]. The bounds established by Jeitschko [26] are largely confirmed although there are several exceptions ($Yb_2(Pb,Ga)$ [84,86], $Pu_2Pt$ [87], $Ca_2Hg$ [63], $Rh_2Ta$ [64], $Zr_2Al$ [75], and $SrF_2$ [14]) that fall outside the established boundaries to varying degrees (Fig. 13). The location of these compounds in lattice parameter ratio space provides evidence that the $(a+c)/b$ ratio defining the $Co_2Si$-type phase may extend to larger values.

Our measured and calculated $PbF_2$ lattice parameters as a function of pressure are in general agreement with previous data [5]. Upon compression, the lattice parameter ratios of $PbF_2$ begin to evolve from the cotunnite field toward the $Co_2Si$ field (Fig. 13). The anomalous lattice compressibility observed from 10-22 GPa generally corresponds to the region where the lattice parameter ratios adopt values that are intermediate between the cotunnite and $Co_2Si$ regions. Above 22 GPa, the $a/c$ ratio becomes consistent with $Co_2Si$ values, but the $(a+c)/b$ ratio at these pressures falls in the range of 3.50-3.55, which is larger than the previously defined boundary of the $Co_2Si$-type phase [5,13,26]. The bonding analysis described above shows that the high-

pressure phase of $PbF_2$ does indeed have a $Co_2Si$-type structure. The empirical boundaries defining phases based on lattice parameter ratios of Jeitschko [26] should thus be modified with the $Co_2Si$ field expanded to a wider range of lattice constant ratio. Consequently, we propose to extend the boundary describing $Co_2Si$-type phases including those under compression to values of $(a+c)/b$ from 3.1 to 3.55 (Fig. 13).

To enable comparison to the lattice cell parameter ratios of cotunnite- and $Co_2Si$-type $PbF_2$, the $Ni_2In$-type structure can be represented by an orthorhombic unit cell according to Léger *et al*. [13]: $a = c_h$, $b = a_h$, and $c = \sqrt{3}a_h$, where h refers to the hexagonal lattice parameters, and the orthorhombic lattice parameters are given without subscripts. In the coordinates of Fig. 13, the $Ni_2In$-type phase then describes a straight line given by:

$$\frac{a}{c} = \frac{1}{\sqrt{3}}\frac{a+c}{b} - 1.$$

Based on our literature survey, $Ni_2In$-type compounds adopt orthorhombic *a/c* values of 0.69 to 0.775. At high temperature, the unit cell of the $PbF_2$ hexagonal phase falls as expected on this line (Fig. 13). The $Ni_2In$-type alkaline earth fluorides, $CaF_2$, $SrF_2$ and $BaF_2$ exhibit slightly smaller orthorhombic *a/c* values than $Ni_2In$-type $PbF_2$ [14]. It is notable that the $PbF_2$ lattice parameter ratios evolve with pressure away from the $Ni_2In$ stability region, consistent with the stability of the $Co_2Si$-type $PbF_2$ to higher pressure than in the alkaline earth fluorides.

Alkaline earth difluorides such as $SrF_2$ also evolve with application of pressure. Above 20 GPa, the lattice parameters of $SrF_2$ move out of the cotunnite stability field, and by 28.4 GPa adopt lattice parameter ratios consistent with the $Co_2Si$-type phase [14]. Unlike $PbF_2$, $SrF_2$ appears to evolve toward the $Ni_2In$-type line with increasing pressure at room temperature, eventually transforming to the $Ni_2In$-type phase [14].

### E. Comparison with lanthanide and actinide dioxides

Several theoretical studies have recently reported the compression behavior to megabar pressures of several $AO_2$ materials including $CeO_2$, $ThO_2$, $UO_2$, and $PuO_2$ [18–20,25]. These first-principles DFT calculations show that all four compounds undergo isostructural phase transitions starting from an orthorhombic cotunnite-type structure with continuous evolution of lattice parameters.

$CeO_2$ and $ThO_2$ isosymmetrically transform from a 9-coordinated cotunnite-type *Pnma* to an unspecified 10-coordinated type at pressures above 1 Mbar [19]. Both materials exhibit anomalous changes in lattice parameters similar to what we observe in $PbF_2$, with enhanced compression along *a* and reduced or negative compression along *b* and *c*. The transition region ranges from 106-160 GPa in $CeO_2$ and from 80-130 GPa in $ThO_2$. Figure 13 shows the variation in lattice parameter ratios for $ThO_2$ with compression. The lattice parameter ratios evolve away from cotunnite values and approach but do not cross into the $Co_2Si$-type field. The high-pressure *Pnma*-phase for these materials is described as an orthorhombic distortion of the $Ni_2In$-type ($P6_3/mmc$) structure, which is consistent with the final value of lattice parameter ratios in Fig. 13.

In case of $UO_2$ and $PuO_2$ [18], the pressure-enthalpy curve of the *Pnma* has 3 distinct regions, *Pnma*-I or cotunnite, followed by *Pnma-II* at P > 90 GPa and *Pnma-III* at P > 120 GPa. The *Pnma-II* phase has a $Co_2Si$-type structure and was identified by the anomalous behavior of the lattice parameters (the same as $PbF_2$ in Fig. 4), while the *Pnma-III* phase is described as structurally degenerate with symmetry of either *Cmcm* or $Cmc2_1$. The lattice parameter ratios of $UO_2$ and $PuO_2$ are consistent with the $Co_2Si$ range at high pressures, unlike $CeO_2$ and $ThO_2$ (Fig. 13).

The ultra-high-pressure phase of all the four compounds resembles an orthorhombic distortion of the $Ni_2In$-type: the lattice parameter ratios approach the line that defines the $Ni_2In$-type structure but do not fall directly on it at any pressure calculated. $UO_2$ and $PuO_2$ form centrosymmetric structures at P ~ 120 GPa (either *Cmcm* or *Cmc*$2_1$, with 11-fold coordination, where *Cmcm* is a supergroup of *Pnma* and *Cmc*$2_1$ is a subgroup of *Cmcm*), while $CeO_2$ and $ThO_2$ transform into a distorted $Ni_2In$-type phase with *Pnma* space group at P > 160 GPa and > 130 GPa respectively. Unlike the oxides, with increasing pressure the lattice parameter ratios of $PbF_2$ remain within the $Co_2Si$ field to the uppermost limit of this study (70 GPa using DFT and 75 GPa experimentally) and the hexagonal $Ni_2In$-type phase is formed only on heating or under highly non-hydrostatic conditions. Experimental studies have not yet verified the isosymmetric phase transition in the actinide and lanthanide oxides and are required to confirm the lattice parameter trends predicted theoretically. Our results show that isosymmetric phase transitions may be an important aspect of high-pressure behavior in $AX_2$ materials.

## V. CONCLUSIONS

The behavior of $PbF_2$ under compression was investigated experimentally in the diamond anvil cell by x-ray diffraction to pressures of 75 GPa at room temperature and to 64.5 GPa and temperatures up to 2430 K , as well as through first-principles DFT calculations at 0 K and up to 70 GPa. The variation of the lattice parameters with pressure is characterized by two monotonic compression regions where the cotunnite and post-cotunnite structures are stable (below 10 GPa and above 22 GPa, respectively) with an intermediate anisotropic compression zone between them. We have shown computationally that α-$PbF_2$ undergoes a pressure-induced isosymmetric phase transition to a post-cotunnite $Co_2Si$-type structure through consideration of atomic

distances and bonding changes with compression. The intermediate zone at 10-22 GPa is characterized by continuous atomic rearrangements whereby a $10^{th}$ fluorine atom, which distinguishes the $Co_2Si$ structure from the cotunnite structure, approaches the cotunnite coordination polyhedron and then finally establishes a bond at ~22 GPa. Valence electron density calculations are also consistent with bond formation at this pressure.

The high-pressure behavior of $PbF_2$ is also examined in the context of lattice parameter systematics for $AX_2$ compounds. The transition region from 10-22 GPa corresponds to lattice parameter ratios intermediate between those characteristic of the cotunnite-type phase and the $Co_2Si$-type phase. We show that existing systematics for the $Co_2Si$ phase need to be revised to account for the high-pressure behavior of $PbF_2$ based both on empirical observations and theoretical calculations.

Upon laser heating above 25.9 GPa, the $Co_2Si$-type phase begins to transform to the hexagonal, 11-coordinated, $Ni_2In$-type. This phase disappears completely upon temperature quench, suggestive of a negative Clapeyron slope for the phase transition. Upon heating at higher pressures, the fraction of the $Ni_2In$-type phase continues to grow until almost complete transformation is observed at 43 GPa. Upon temperature quench, the sample either completely or partially converted back to $Co_2Si$-type throughout the pressure range of the experiment (up to 65.4 GPa). $PbF_2$ shows distinct differences from the behavior of the alkaline earth fluorides as well as lanthanide and actinide dioxides and provides an example of a novel pathway for transformations among highly coordinated $AX_2$ compounds.

## ACKNOWLEDGEMENTS

We thank Greg Finkelstein and Earl O'Bannon for experimental assistance and helpful discussion. This work was supported by the NSF. Use of the Advanced Photon Source, an Office of Science User Facility operated for the U.S. Department of Energy (DOE) Office of Science by Argonne National Laboratory, was supported by the U.S. DOE under Contract No. DE-AC02-06CH11357. We acknowledge the support of GeoSoilEnviroCARS (Sector 13), which is supported by the National Science Foundation - Earth Sciences (EAR-1128799), and the Department of Energy, Geosciences (DE-FG02-94ER14466).

## VI. REFERENCES

1. J. Haines and J.M. Léger, Eur. J. Solid State Inorg. Chem. **37**, 785 (1997).

2. G.A. Samara, J. Phys. Chem. Solids **40**, 509 (1979).

3. M. Fujita, M. Itoh, Y. Bokumoto, H. Nakagawa, D.L. Alov, and M. Kitaura, Phys. Rev. B **61**, 15731 (2000).

4. H. Jiang, R. Orlando, M.A. Blanco, and R. Pandey, J. Phys. Condens. Matter **16**, 3081 (2004).

5. J. Haines, J.M. Léger, and O. Schulte, Phys. Rev. B **57**, 7551 (1998).

6. H.E. Lorenzana, J.E. Klepeis, M.J. Lipp, W.J. Evans, H.B. Radousky, and M. Van Schilfgaarde, Phys. Rev. B **56**, 543 (1997).

7. J. Oberschmidt and D. Lazarus, Phys. Rev. B **21**, 2952 (1980).

8. G.A. Samara, Phys. Rev. B **13**, 4529 (1976).

9. V. Kanchana, G. Vaitheeswaran, and M. Rajagopalan, J. Alloys Compd. **359**, 66 (2003).

10. H. Shi, W. Luo, B. Johansson, and R. Ahujia, J. Phys. Condens. Matter **21**, 415501 (2009).

11. L. Gerward, J.S. Olsen, S. Steenstrup, M. Malinowski, S. Åsbrink, and A. Waskowska, J. Appl. Crystallogr. **25**, 578 (1992).

12. S. Speziale and T.S. Duffy, Phys. Chem. Miner. **29**, 465 (2002).

13. J.M. Léger, J. Haines, A. Atouf, O. Schulte, and S. Hull, Phys. Rev. B **52**, 13247 (1995).

14. S.M. Dorfman, F. Jiang, Z. Mao, A. Kubo, Y. Meng, V.B. Prakapenka, and T.S. Duffy, Phys. Rev. B **81**, 174121 (2010).

15. A.R. Oganov, M.J. Gillan, and G.D. Price, Phys. Rev. B **71**, 64104 (2005).

16. K. Umemoto, R.M. Wentzcovitch, and P.B. Allen, Science **311**, 983 (2006).

17. T. Duffy, N. Madhusudhan, and K.K.M. Lee, in *Treatise Geophys.*, edited by G. Schubert, 2nd ed. edited by edited by G. Schubert (Elsevier, Oxford, 2015), pp. 149–178.

18. H.X. Song, H.Y. Geng, and Q. Wu, Phys. Rev. B **85**, 64110 (2012).

19. H.X. Song, L. Liu, H.Y. Geng, and Q. Wu, Phys. Rev. B **87**, 184103 (2013).

20. B.-T. Wang, H. Shi, W.-D. Li, and P. Zhang, J. Nucl. Mater. **399**, 181 (2010).

21. L.S. Dubrovinsky, N.A. Dubrovinskaia, V. Swamy, J. Muscat, N.M. Harrison, R. Ahuja, B. Holm, and B. Johansson, Nature **410**, 653 (2001).

22. B. Grocholski, S.-H. Shim, E. Cottrell, and V.B. Prakapenka, Am. Mineral. **99**, 170 (2014).

23. S.R. Shieh, A. Kubo, T.S. Duffy, V.B. Prakapenka, and G. Shen, Phys. Rev. B **73**, (2006).

24. Y. Al-Khatatbeh, K.K.M. Lee, and B. Kiefer, Phys. Rev. B **79**, (2009).

25. H.Y. Geng, Y. Chen, Y. Kaneta, and M. Kinoshita, Phys. Rev. B **75**, 54111 (2007).

26. W. Jeitschko, Acta Crystallogr. Sect. B **24**, 930 (1968).

27. A. Costales, M.A. Blanco, R. Pandey, and J.M. Recio, Phys. Rev. B **61**, 11359 (2000).

28. B.G. Hyde, M. O'Keeffe, W.M. Lyttle, and N.E. Brese, Acta Chem. Scand. **46**, 216 (1992).

29. A.P. Hammersley, S.O. Svensson, M. Hanfland, A.N. Fitch, and D. Hausermann, High Press. Res. **14**, 235 (1996).

30. C. Prescher and V.B. Prakapenka, High Press. Res. **35**, 223 (2015).

31. V.B. Prakapenka, A. Kubo, A. Kuznetsov, A. Laskin, O. Shkurikhin, P. Dera, M.L. Rivers, and S.R. Sutton, High Press. Res. **28**, 225 (2008).

32. T.J.B. Holland and S.A.T. Redfern, Mineral. Mag. **61**, 65 (1997).

33. Y. Fei, A. Ricolleau, M. Frank, K. Mibe, G. Shen, and V. Prakapenka, Proc. Natl. Acad. Sci. **104**, 9182 (2007).

34. R.J. Angel, J. Gonzalez-Platas, and M. Alvaro, Z. Für Krist. **229**, 405 (2014).

35. P. Hohenberg and W. Kohn, Phys. Rev. **136**, B864 (1964).

36. W. Kohn and L.J. Sham, Phys. Rev. **140**, A1133 (1965).

37. S.J. Clark, M.D. Segall, C.J. Pickard, P.J. Hasnip, M.I.J. Probert, K. Refson, and M.C. Payne, Z. Für Krist. **220**, 567 (2005).

38. D. Vanderbilt, Phys. Rev. B **41**, 7892 (1990).

39. D.M. Ceperley and B.J. Alder, Phys. Rev. Lett. **45**, 566 (1980).

40. H.J. Monkhorst and J.D. Pack, Phys. Rev. B **13**, 5188 (1976).

41. R. Fletcher, *Practical Methods of Optimization*, (Wiley & Sons, Inc., New York, NY, 1987), 2nd ed.

42. L. Ehm, K. Knorr, F. Mädler, H. Voigtländer, E. Busetto, A. Cassetta, A. Lausi, and B. Winkler, J. Phys. Chem. Solids **64**, 919 (2003).

43. A. Dubinin, B. Winkler, K. Knorr, and V. Milman, Eur. Phys. J. B-Condens. Matter Complex Syst. **39**, 27 (2004).

44. A. van de Walle and G. Ceder, Phys. Rev. B **59**, 14992 (1999).

45. D.-M. Wee and T. Suzuki, Trans. Jpn. Inst. Met. **20**, 634 (1979).

46. S. Klotz, J.-C. Chervin, P. Munsch, and G. Le Marchand, J. Phys. Appl. Phys. **42**, 75413 (2009).

47. M.O. Manasreh and D.O. Pederson, Phys. Rev. B **30**, 3482 (1984).

48. J.S. Smith, S. Desgreniers, J.S. Tse, J. Sun, D.D. Klug, and Y. Ohishi, Phys. Rev. B **79**, (2009).

49. A.F. Andresen, A.J. Maeland, and D. Slotfeldt-Ellingsen, J. Solid State Chem. **20**, 93 (1977).

50. M. Enomoto, J. Phase Equilibria **12**, 363 (1991).

51. E. Ganglberger, H. Nowotny, and F. Benesovsky, Monatshefte Chem. Verwandte Teile Anderer Wiss. **98**, 95 (1967).

52. S. Geller and V. Wolontis, Acta Crystallogr. **8**, 83 (1955).

53. A.B. Gokhale and R. Abbaschian, Bull. Alloy Phase Diagr. **11**, 460 (1990).

54. K.A. Gschneidner and F.W. Calderwood, Bull. Alloy Phase Diagr. **9**, 673 (1988).

55. K.A. Gschneidner and F.W. Calderwood, Bull. Alloy Phase Diagr. **9**, 676 (1988).

56. K.A. Gschneidner and F.W. Calderwood, Bull. Alloy Phase Diagr. **9**, 680 (1988).

57. K.A. Gschneidner and F.W. Calderwood, Bull. Alloy Phase Diagr. **9**, 684 (1988).

58. K.A. Gschneidner and F.W. Calderwood, Bull. Alloy Phase Diagr. **10**, 28 (1989).

59. K.A. Gschneidner and F.W. Calderwood, Bull. Alloy Phase Diagr. **10**, 31 (1989).

60. K.A. Gschneidner and F.W. Calderwood, Bull. Alloy Phase Diagr. **10**, 37 (1989).

61. K.A. Gschneidner and F.W. Calderwood, Bull. Alloy Phase Diagr. **10**, 40 (1989).

62. K.A. Gschneidner and F.W. Calderwood, Bull. Alloy Phase Diagr. **10**, 44 (1989).

63. C. Guminski, J. Phase Equilibria **14**, 90 (1993).

64. K.P. Gupta, J. Phase Equilibria **24**, 575 (2003).

65. M. Idiri, T. Le Bihan, S. Heathman, and J. Rebizant, Phys. Rev. B **70**, 14113 (2004).

66. K. Ishida and T. Nishizawa, Bull. Alloy Phase Diagr. **11**, 555 (1990).

67. V.P. Itkin and C.B. Alcock, Bull. Alloy Phase Diagr. **10**, 630 (1989).

68. V.P. Itkin and C.B. Alcock, J. Phase Equilibria **13**, 162 (1992).

69. K. Kinoshita, M. Nishimura, Y. Akahama, and H. Kawamura, Solid State Commun. **141**, 69 (2007).

70. Y. Li, B. Li, T. Cui, Y. Li, L. Zhang, Y. Ma, and G. Zou, J. Phys. Condens. Matter **20**, 45211 (2008).

71. G. Liu, H. Wang, Y. Ma, and Y. Ma, Solid State Commun. **151**, 1899 (2011).

72. T. Matsuoka, H. Fujihisa, N. Hirao, Y. Ohishi, T. Mitsui, R. Masuda, M. Seto, Y. Yoda, K. Shimizu, A. Machida, and K. Aoki, Phys. Rev. Lett. **107**, 25501 (2011).

73. A.J. McAlister, Bull. Alloy Phase Diagr. **7**, 368 (1986).

74. J.L. Murray, Bull. Alloy Phase Diagr. **6**, 327 (1985).

75. J. Murray, A. Peruzzi, and J.P. Abriata, J. Phase Equilibria **13**, 277 (1992).

76. P. Nash and A. Nash, Bull. Alloy Phase Diagr. **8**, 6 (1987).

77. A. Nash and P. Nash, Bull. Alloy Phase Diagr. **8**, 255 (1987).

78. D. Nishio-Hamane, H. Dekura, Y. Seto, and T. Yagi, Phys. Chem. Miner. **42**, 385 (2014).

79. H. Okamoto, Bull. Alloy Phase Diagr. **11**, 404 (1990).

80. H. Okamoto, Bull. Alloy Phase Diagr. **11**, 574 (1990).

81. A. Palenzona and S. Cirafici, J. Common Met. **63**, 105 (1979).

82. A. Palenzona and S. Cirafici, Bull. Alloy Phase Diagr. **10**, 234 (1989).

83. A. Palenzona and S. Cirafici, Bull. Alloy Phase Diagr. **11**, 493 (1990).

84. A. Palenzona and S. Cirafici, J. Phase Equilibria **12**, 479 (1991).

85. A. Palenzona and S. Cirafici, J. Phase Equilibria **12**, 482 (1991).

86. A. Palenzona and S. Cirafici, J. Phase Equilibria **13**, 32 (1992).

87. D.E. Peterson, Bull. Alloy Phase Diagr. **10**, 474 (1989).

88. J. Sangster and A.D. Pelton, J. Phase Equilibria **18**, 78 (1997).

89. J. Sangster and A.D. Pelton, J. Phase Equilibria **18**, 173 (1997).

90. D. Santamaria-Perez, A. Vegas, C. Muehle, and M. Jansen, Acta Crystallogr. B **67**, 109 (2011).

91. K.J. Schulz, O.A. Musbah, and Y.A. Chang, J. Phase Equilibria **12**, 10 (1991).

92. M.F. Singleton and P. Nash, Bull. Alloy Phase Diagr. **9**, 592 (1988).

93. J.S. Smith, S. Desgreniers, D.D. Klug, and J.S. Tse, Solid State Commun. **149**, 830 (2009).

94. J.S. Smith, S. Desgreniers, J.S. Tse, and D.D. Klug, J. Appl. Phys. **102**, 43520 (2007).

95. R.C. Sharma, T.L. Ngai, and Y.A. Chang, Bull. Alloy Phase Diagr. **10**, 657 (1989).

96. K. Ishida and T. Nishizawa, J. Phase Equilibria **12**, 77 (1991).

97. P. Boldrini and B.O. Loopstra, Acta Crystallogr. **22**, 744 (1967).

## VII. FIGURES

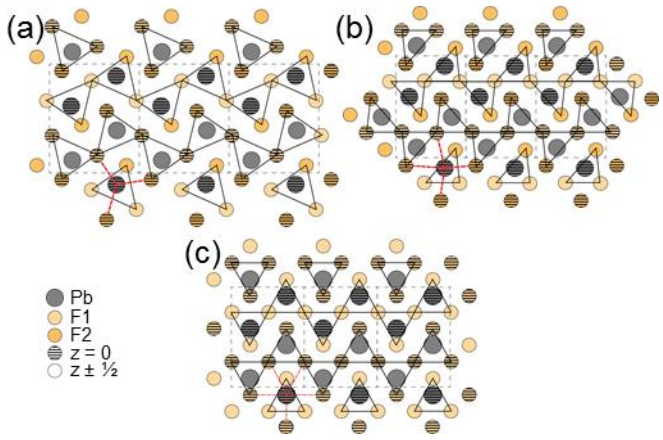


FIG 1. Projections of the a. cotunnite b. $Co_2Si$ and c. hexagonal $Ni_2In$ structures along the *b* axis in orthorhombic coordinates. Trigonal prisms are shown as triangles. Orthorhombic unit cells are represented by dashed boxes. Red dashed lines indicate the bonds between the central Pb atom and the triangular prism caps. In the case of cotunnite and $Co_2Si$, the two crystallographically distinct F sites are denoted as F1 and F2

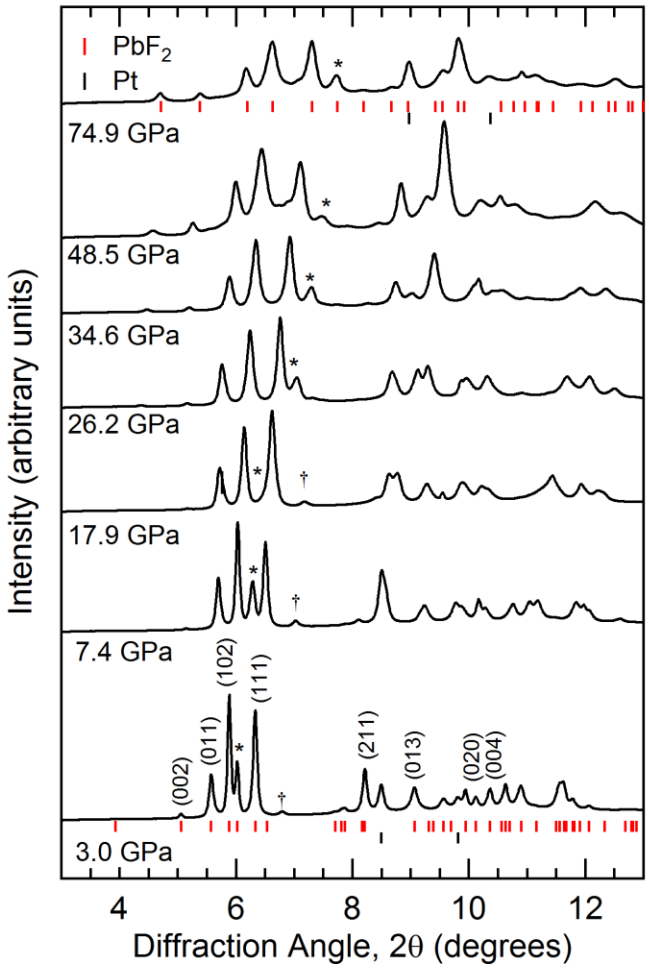


FIG. 2. Representative x-ray diffraction patterns of $PbF_2$ as a function of pressure. Red tick marks indicate cotunnite-/$Co_2Si$-type diffraction peak locations, black tick marks indicate Pt peaks. Miller indices (*hkl*) of selected $PbF_2$ peaks are shown. Asterisk (*) tracks the (200) peak of $PbF_2$. Dagger (†) indicates peak from Pb impurity.

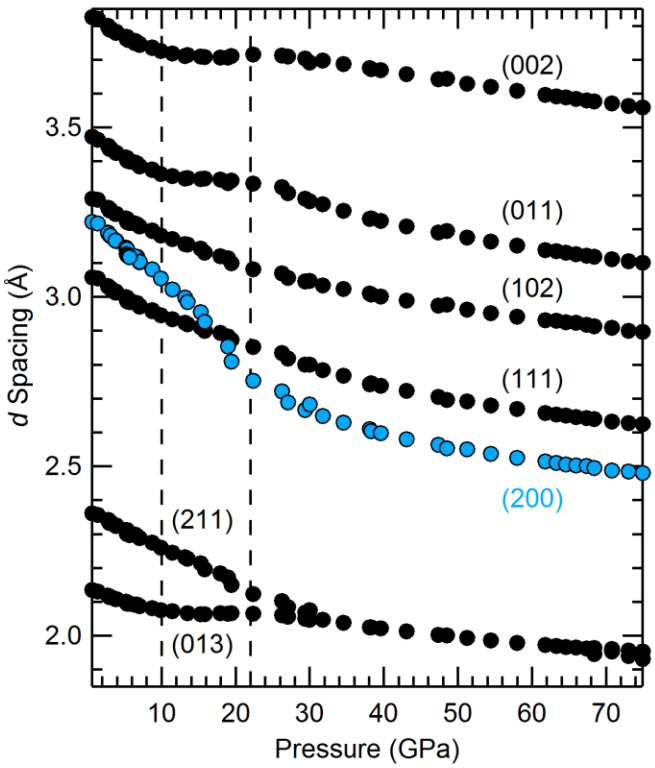


FIG. 3. Measured *d*-spacings of selected $PbF_2$ peaks up to 75 GPa. The (200) peak is shown in blue to highlight its unusual compressibility.

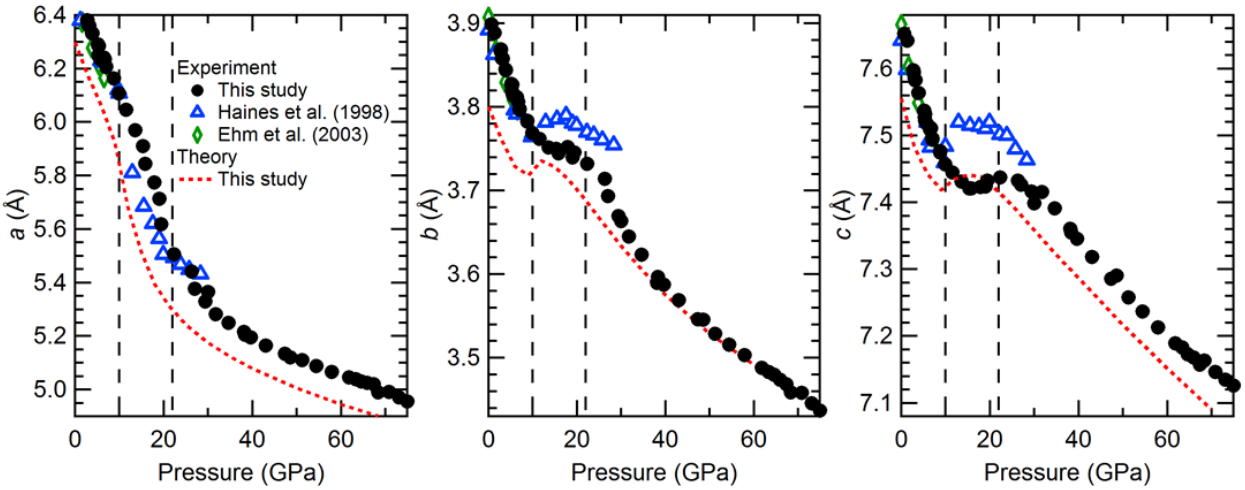


FIG. 4. Lattice parameters as a function of pressure for $PbF_2$. Dashed black vertical lines mark the transition region.

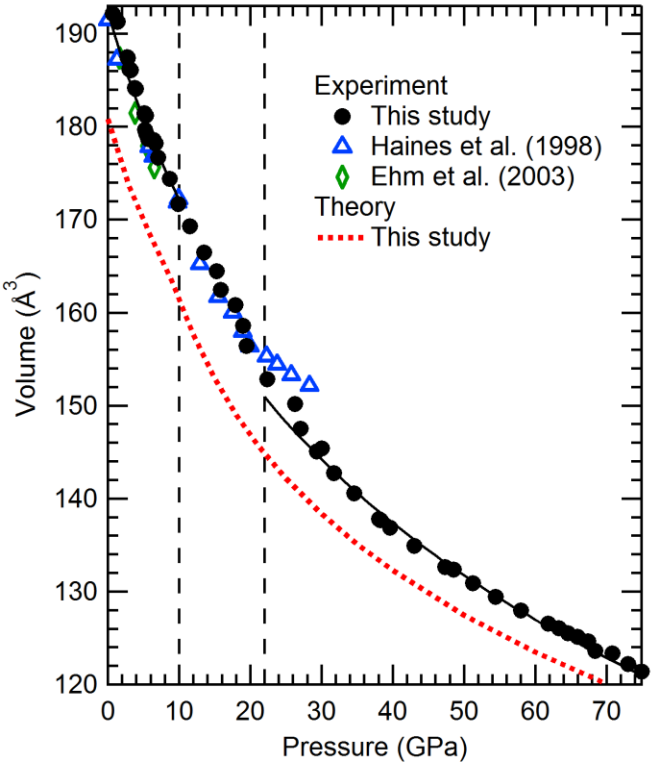


FIG. 5. Unit cell volume of $PbF_2$ as a function of pressure. Solid lines represent the equation of state fits. Symbols are the same as in Fig. 3.

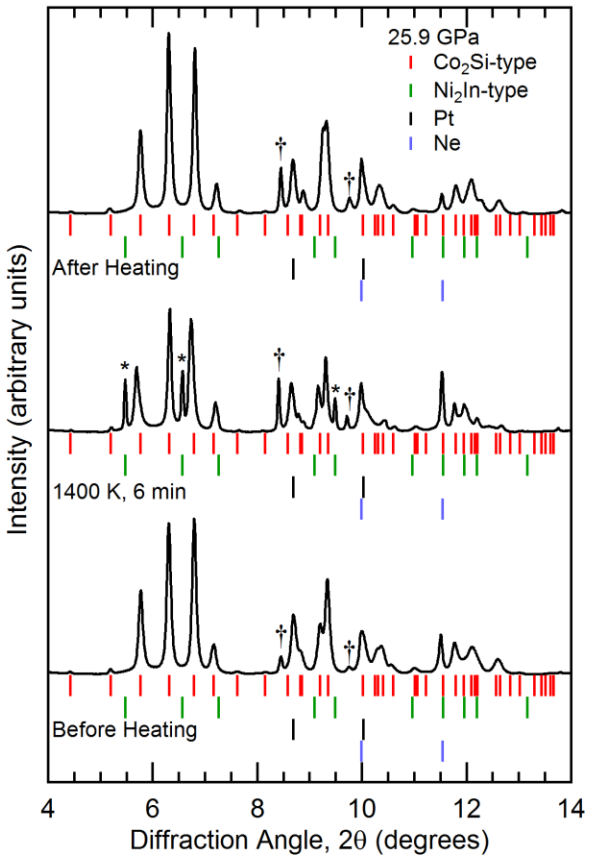


FIG. 6. High pressure-temperature x-ray diffraction patterns for $PbF_2$ from heating experiment at 25.9 GPa. Tick marks indicate expected peak locations for $Co_2Si$-type phase (red, $a$ = 5.329(5) Å, $b$ = 3.788(5) Å, $c$ = 7.363(7) Å), $Ni_2In$-type phase (green, $a$ = 4.042 Å, $c$ = 5.285 Å), platinum (black), and neon (blue). Asterisks (*) indicate new $Ni_2In$-type peaks emerging upon heating and daggers (†) mark the location of $Pt_3Pb$ alloy peaks.

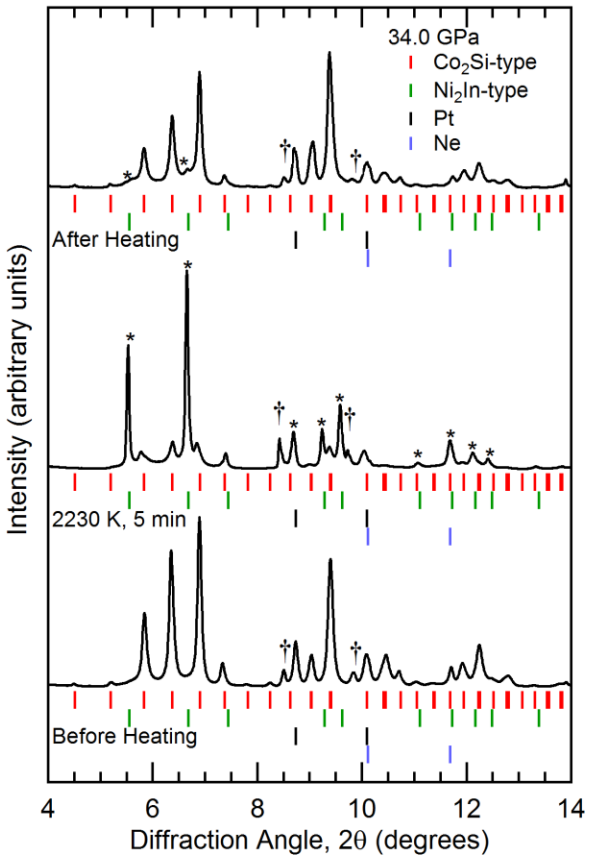


FIG. 7. X-ray diffraction pattern from heating experiment at 34.0 GPa. $Ni_2In$ becomes the dominant phase at high temperature, although $Co_2Si$-type peaks do not completely disappear. Upon quench (upper trace), the two weak $Ni_2In$ peaks are retained with low intensity at $2\theta = 5.6°$ and 6.6°. The high-temperature lattice parameters of the $Ni_2In$-type phase are: $a$ = 4.001(1) Å, $c$ = 5.182(2) Å.

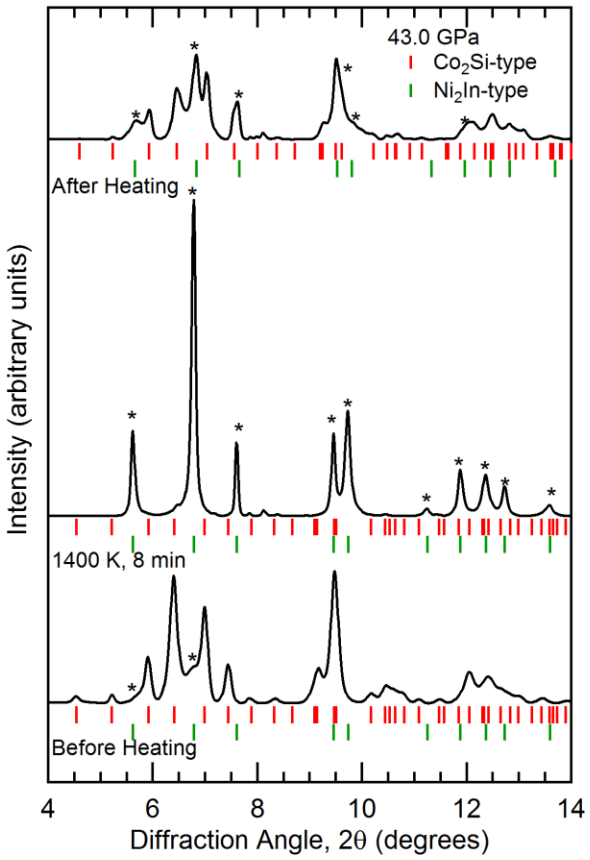


FIG. 8. X-ray diffraction pattern from heating experiment at 43 GPa. Nearly complete transformation to $Ni_2In$ is observed at high temperature but a mixture of both phases is observed upon quench. $Ni_2In$ is fit with $a$ = 3.942(1) Å and $c$ = 5.044(2) Å.

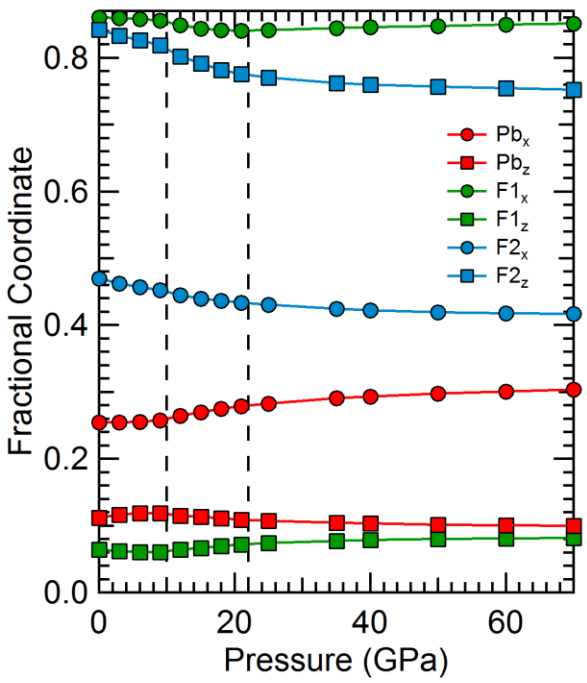


FIG. 9. Change in fractional coordinates with pressure. Pb, F1 and F2 are the lead and two flourine atoms respectively. Subscripts indicate coordinate directions.

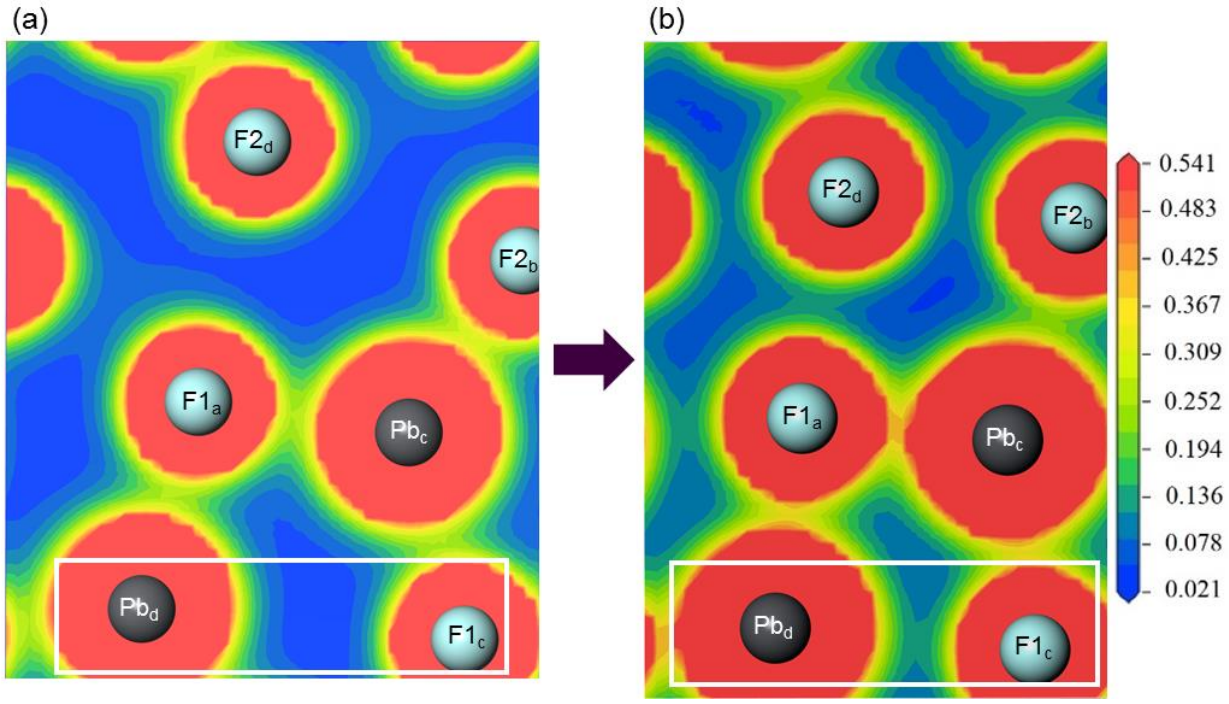

FIG. 10. Total electron density (e/Å$^3$) of $PbF_2$ in the (010) plane at a. 0 GPa and b. 25 GPa. The white box indicates the $Pb_d$-$F1_c$ bond (crystallographically equivalent to $Pb_a$-$F1_{b2}$) which, when formed, indicates transition to the $Co_2Si$-type phase.

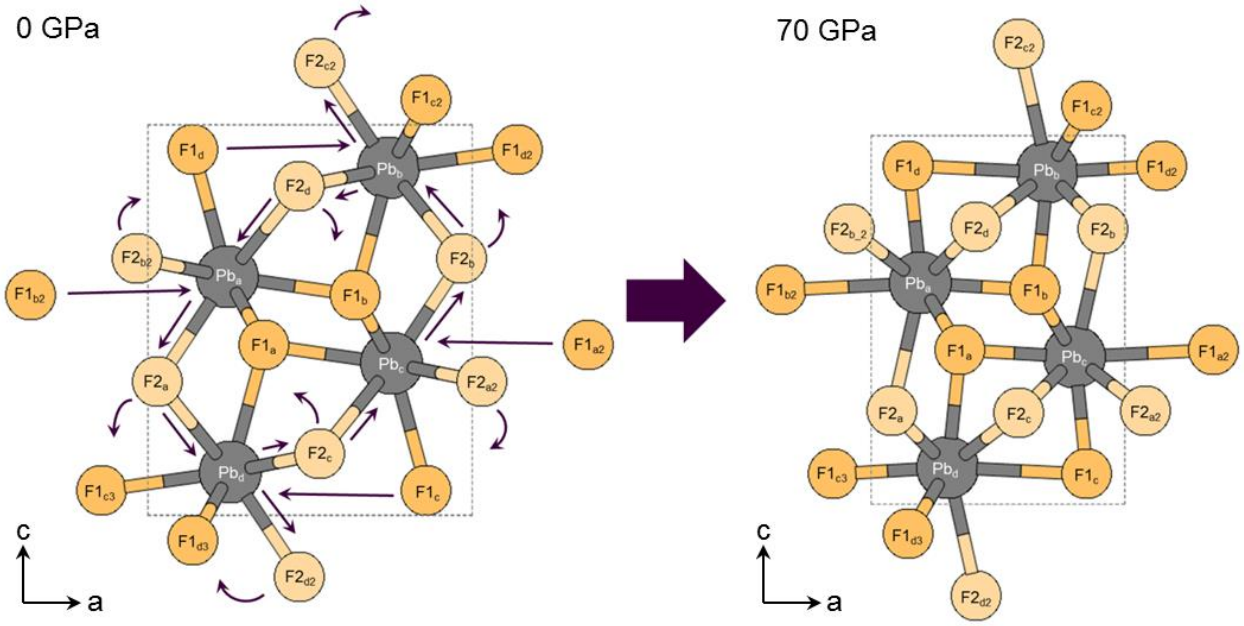


FIG. 11. Atomic level structural evolution of $PbF_2$ with compression. Pb atoms are in gray, F atoms are in orange. The different shades of orange indicate the two different crystallographic sites of F (F1 and F2). Arrows indicate the direction of atomic movement.

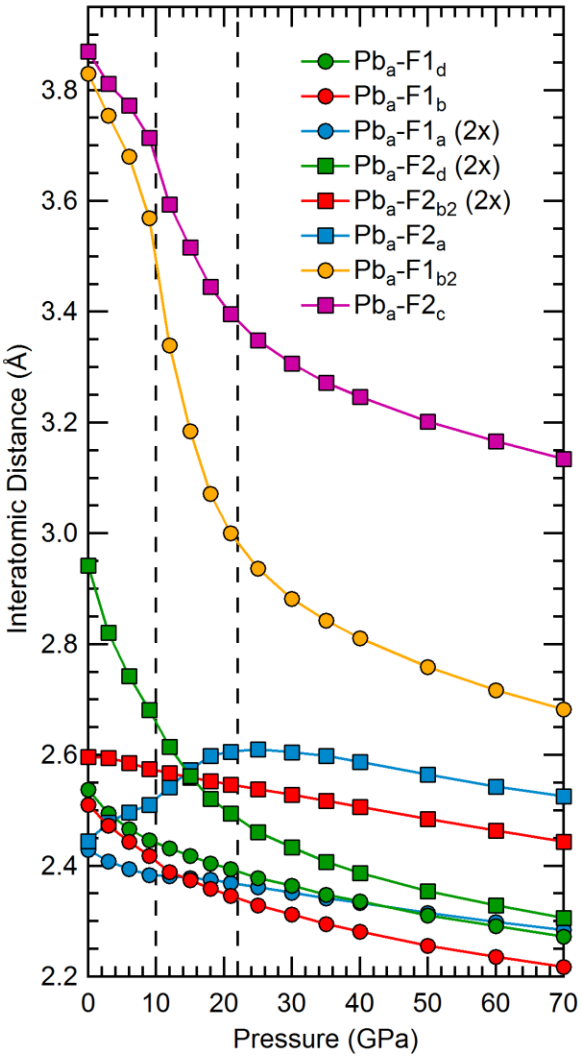


FIG. 12. Calculated interatomic distances of $PbF_2$ as a function of pressure.

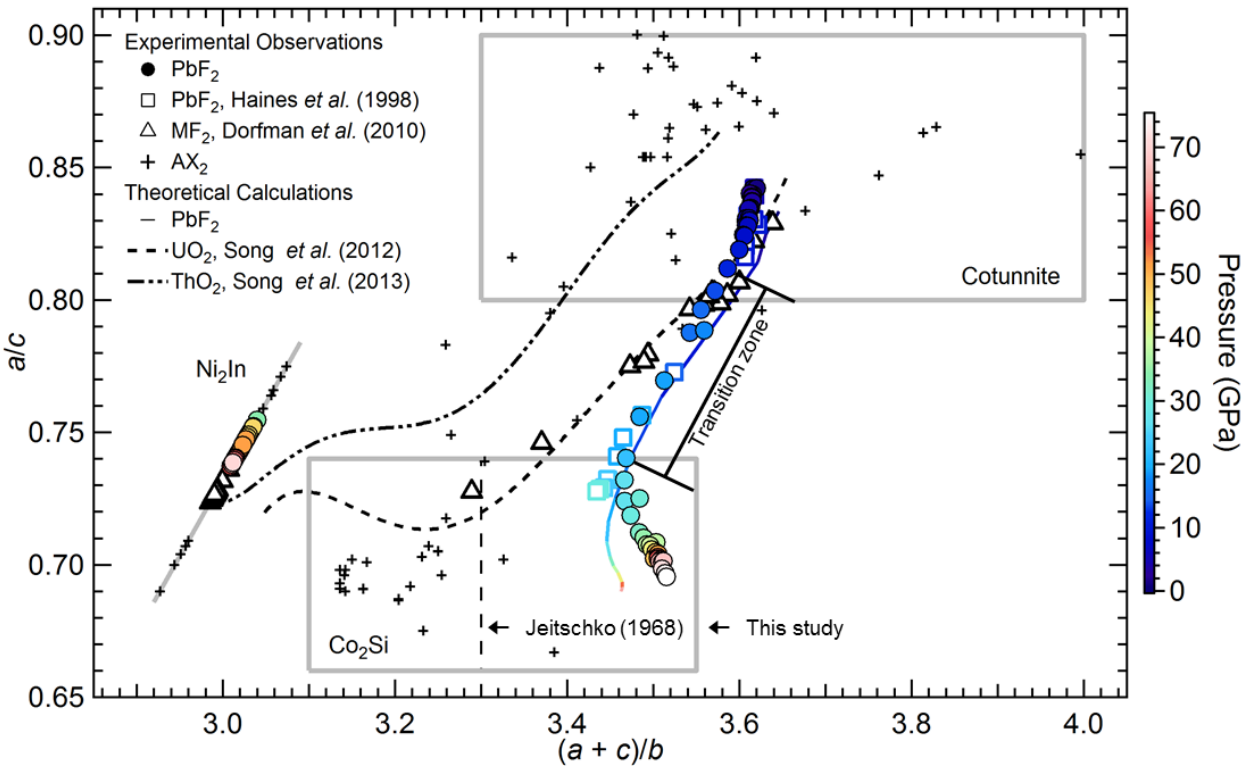


FIG. 13. Selected $AX_2$ compounds plotted as a function of lattice parameter ratios. $PbF_2$ data are contoured by color to indicate pressure. Crosses show data from binary compounds at room pressure [5,14,26,48–96]. Transition region denotes the pressure range from 10-22 GPa where anomalous changes in lattice parameter and volume compressibility are observed (Fig. 4, 5). The dotted black lines are polynomial fits to the $AO_2$ data of Song *et al*. [18,19]. The solid gray lines show the boundaries of the cotunnite and $Co_2Si$-type fields, as well as the linear relationship defining $Ni_2In$-type compounds. The lattice parameters ratios defining the $Co_2Si$-type field have been expanded (from dashed to solid boundary) to encompass lattice parameter ranges observed in $PbF_2$.

## VIII. TABLES

Table I. Lattice parameters and atomic positions of α-$PbF_2$ at ambient conditions. All atoms are at y = 0.25.

| Reference | Lattice Parameters (Å) | | | Atomic positions | | | | | |
|---|---|---|---|---|---|---|---|---|---|
| | *a* | *b* | *c* | $Pb_x$ | $Pb_z$ | $F1_x$ | $F1_z$ | $F2_x$ | $F2_z$ |
| This study[a] | 6.4472(3) | 3.9019(2) | 7.6514(3) | | | | | | |
| This study[b] | 6.298 | 3.800 | 7.556 | 0.25469 | 0.11149 | 0.86023 | 0.06450 | 0.46994 | 0.84235 |
| Boldrini and Loopstra [97][c] | 6.440 | 3.899 | 7.651 | 0.2527 | 0.1042 | 0.8623 | 0.0631 | 0.4622 | 0.8457 |
| Haines et al. [5][b] | 6.444 | 3.900 | 7.648 | | | | | | |

a. x-ray diffraction experiment

b. theoretical calculation

c. neutron diffraction experiment

TABLE II. Equation of state parameters for $PbF_2$.

| Reference | $V_0$ (Å$^3$) | $K_0$ (GPa) | $K_0$' |
|---|---|---|---|
| | Cotunnite-type | | |
| This study (Exp.) | 192.48(1)* | 72(3) | 4* |
| This Study (Theory) | 180.82 | 68.0 | 4 |
| Haines *et al*. (1998) | 192.6(3) | 66(7) | 7(3) |
| | $Co_2Si$-type | | |
| This study (Exp.) | 182(2) | 81(4) | 4* |

Asterisk (*) indicates fixed values.